

ARTICLE TYPE

Locally Adaptive Non-Hydrostatic Shallow Water Extension for Moving Bottom-Generated Waves

Kemal Firdaus*^{1,2} | Jörn Behrens^{1,2}¹Department of Mathematics, Universität Hamburg, Bundesstrasse 53-55, 20146 Hamburg, Germany²Center for Earth System Research and Sustainability (CEN), Universität Hamburg, Bundesstrasse 53-55, 20146 Hamburg, Germany**Correspondence***Kemal Firdaus, Department of Mathematics, Universität Hamburg, Bundesstrasse 53-55, 20146 Hamburg, Germany.
Email: kemal.firdaus@uni-hamburg.de**Abstract**

We propose a locally adaptive non-hydrostatic model and apply it to wave propagation generated by a moving bottom. This model is based on the non-hydrostatic extension of the shallow water equations (SWE) with a quadratic pressure relation, which is suitable for weakly dispersive waves. The approximation is mathematically equivalent to the Green-Naghdi equations. Applied globally, the extension requires solving an elliptic system of equations in the whole domain at each time step. Therefore, we develop an adaptive model that reduces the application area of the extension and by that the computational time. The elliptic problem is only solved in the area where the dispersive effect might play a crucial role. To define the non-hydrostatic area, we investigate several potential criteria based on the hydrostatic SWE solution. We validate and illustrate how our adaptive model works by first applying it to simulate a simple propagating solitary wave, where exact solutions are known. Following that, we demonstrate the accuracy and efficiency of our approach in more complicated cases involving moving bottom-generated waves, where measured laboratory data serve as reference solutions. The adaptive model yields similar accuracy as the global application of the non-hydrostatic extension while reducing the computational time by more than 50%.

KEYWORDS:

adaptive, non-hydrostatic, dispersive, shallow water equations, moving bottom

1 | INTRODUCTION

Non-hydrostatic pressure is proven to be crucial in some geophysical flow phenomena, including tsunamis caused by landslides¹. Such phenomena can be described as moving bottom-generated waves. The non-hydrostatic pressure yields a wave dispersion effect. Previously proposed models including wave dispersion often involve higher-order derivatives or solving elliptic equations, which demand for more computational resources compared to non-dispersive models. This motivates us to develop an approach, where the dispersive effect is locally and adaptively applied to moving bottom-generated waves.

Depth-averaged models are commonly used for large-scale ocean modeling due to their simplicity and computational efficiency. Boussinesq-type equations are a popular choice for depth-averaged models that can handle the dispersive effect. This model type has been widely used in tsunami research, especially for moving-bottom generated waves^{2,3,4,5,6}. It is derived based on asymptotic expansion on the velocity potential, where different expansion orders lead to various Boussinesq-type equations^{7,8,9,10}. However, such models involve higher-order and sometimes mixed time-space derivatives, which often cause numerical and computational challenges.

Another widely used modeling approach is given by the shallow water equations (SWE), involving only first-order derivatives, simplifying the solution. Despite their capability to describe a wide range of wave dynamics, SWE are limited to the hydrostatic assumption, excluding dispersive effects. Previous research proposed to extend the SWE by including a non-hydrostatic pressure term. To derive such an extension, approximations to the non-hydrostatic pressure and the vertical velocity profile need to be defined. Most studies assumed a linear vertical pressure relation^{11,12,13} while also assuming a linear vertical velocity. Alternatively, a quadratic pressure relation was proposed, which is consistent with the linear vertical velocity assumption¹⁴. This latter relation was proven to be equivalent to Boussinesq-type equations, namely the Green-Naghdi equations¹⁵, making it suitable for modeling weakly dispersive waves. Recently, this work was improved, making it solvable with a projection-based method and applicable for moving bottom-generated waves¹⁶.

Applying the extension globally to the SWE requires the solution of an elliptic system of equations over the whole domain at each time step, adding substantial computational effort to the non-hydrostatic SWE solution. Therefore, we propose an adaptive approach, which aims to apply the non-hydrostatic extension – and thus solving the elliptic problem – only locally in the particular area where the non-hydrostatic pressure plays a significant role.

The projection-based method allows us to use the solution from the hydrostatic SWE solver as a predictor, which will then be corrected by solving the extension-related terms. With this principle in mind, we can apply the correction locally. To define these corrected regions, we investigate several potential criteria based on the hydrostatic SWE solver solutions. To validate and illustrate how our model works, we first compare it with an analytical solution of a simple solitary wave. Subsequently, we apply it to simulate moving bottom-generated waves, which are based on two previous laboratory setups. These experiments involved both vertical and horizontal movement.

2 | MATHEMATICAL MODEL

In this study, we use the one-dimensional non-hydrostatic SWE extension, which is also applicable for moving bottom-generated waves¹⁶, written as:

$$h_t + (hu)_x = 0, \quad (1)$$

$$(hu)_t + \left(hu^2 + \frac{g}{2}h^2\right)_x = gh d_x - \frac{1}{\rho}(hp^{nh})_x + \frac{1}{\rho}P^{nh}|_{z=-d}d_x, \quad (2)$$

$$(hw)_t + (huw)_x = \frac{1}{\rho}P^{nh}|_{z=-d}, \quad (3)$$

$$2hw + hu(2d - h)_x + 2hd_t = -h(hu)_x \quad (4)$$

where Eq. 1 is the mass conservation equation, while Eq. 2 and 3 are the horizontal and vertical momentum balance equations respectively. These equations are also completed with the divergence constraint Eq. 4, which is derived from a linear vertical velocity assumption. The fluid thickness is denoted as $h = \eta + d$, considering the surface elevation η and fluid depth d . Meanwhile, u is the depth-averaged horizontal velocity. In contrast to the hydrostatic SWE, this model also involves the depth-averaged vertical velocity w and non-hydrostatic pressure p^{nh} . To enclose this set of equations, a pressure relation needs to be defined. This study uses a quadratic relation that was further developed for moving bottom cases¹⁶, written as:

$$P_{-d}^{nh} = \frac{6}{4 + d_x^2}p^{nh} + \frac{d_x}{4 + d_x^2}(hp^{nh})_x + \phi, \quad (5)$$

with $\phi = \frac{\rho h}{4 + d_x^2}(gd_x\eta_x - d_{tt} - 2ud_{xt} - u^2d_{xx})$. These equations allow us to solve it with a projection method, which further could be used to obtain an adaptive model.

3 | NUMERICAL METHOD

We will briefly discuss how to solve the model as described in the previous section. As mentioned before, we are interested in solving it using a projection method, also known as a predictor-corrector method. This method lets us use the hydrostatic SWE solver solution as the predictor and make a correction by solving the extension terms. The correction itself is not solved explicitly but rather by solving a system of elliptic equations, which will be elaborated on later.

3.1 | Predictor Step

The hydrostatic SWE (Eq. 1, 2, and 3 without non-hydrostatic pressure terms) are discretized with a second-order Runge-Kutta discontinuous Galerkin (RKDG) method. We consider a computational domain $\Omega = [x_l, x_r]$, which is then divided into N uniform intervals $I_i = [x_{i-1}, x_i]$, where $i = 1, 2, \dots, N$, assuming $x_0 = x_l$ and $x_N = x_r$. To formulate the weak DG formulation of the hydrostatic SWE, we multiply it with a test function ϕ and integrate it over an interval, which leads to

$$\int_{I_i} \phi \mathcal{Q}_t dx - \int_{I_i} \phi_x \mathbf{F}(\mathbf{Q}) dx + [\phi \mathbf{F}^*(\mathbf{Q})]_{x_i}^{x_{i+1}} = \int_{I_i} \phi \mathcal{S}(q) dx, \quad (6)$$

where $\mathbf{Q} = (h, hu, hw)^T$ is the unknowns, while the fluxes and sources are denoted by $\mathbf{F}(\mathbf{Q}) = \left(hu, hu^2 + \frac{g}{2} h^2, huw \right)^T$ and $\mathcal{S}(\mathbf{Q}) = (0, ghd_x, 0)^T$ respectively. The communication between neighboring intervals depends on the definition of the numerical interface flux $\mathbf{F}^*(\mathbf{Q})$, which is unique and based on information from both elements. A Riemann solver (in this case, the Rusanov solver) is used as an approximation.

We discretize the solution in space with a piecewise polynomial represented by the nodal Lagrange basis function, which is also used as the test function. In other word, our solution can be approximated as $\mathbf{Q}_h(x, t) = \sum_i (\tilde{\mathbf{Q}}_h)_i(t) \phi_i(x)$. The fluxes and the sources are approximated similarly. This spatial discretization results in a system of ordinary differential equations for the local degrees of freedom, such that

$$\frac{d\tilde{\mathbf{Q}}_h}{dt} = \mathbf{M}^{-1} (\mathbf{D}^T \mathbf{F}(\tilde{\mathbf{Q}}_h) - \mathbf{M} \mathcal{S}(\tilde{\mathbf{Q}}_h)) - [\phi \mathbf{F}^*(\tilde{\mathbf{Q}}_h)]_{x_i}^{x_{i+1}} =: \mathcal{H}(\tilde{\mathbf{Q}}_h), \quad (7)$$

where $\mathbf{M}_{ij} = \int_{I_i} \phi_i \phi_j dx$ and $\mathbf{D}_{ij} = \int_{I_i} \phi_i (\phi_j)_x dx$, and \mathcal{H} represents the evolution operator of the SWE. This last equation can be solved with any time integrator, which in this work is a second-order Heun's scheme, written as

$$\tilde{\mathbf{Q}}_h^{n+1} = \tilde{\mathbf{Q}}_h^n + \frac{\Delta t}{2} \left(\mathcal{H}(\tilde{\mathbf{Q}}_h^n) + \mathcal{H}(\tilde{\mathbf{Q}}_h^*) \right), \quad (8)$$

where the superscript n stands for a discrete time step, and $\tilde{\mathbf{Q}}_h^*$ is derived by one Euler forward step

$$\tilde{\mathbf{Q}}_h^* = \tilde{\mathbf{Q}}_h^n + \Delta t (\mathcal{H}(\tilde{\mathbf{Q}}_h^n)). \quad (9)$$

We mark the results from this middle step with a tilde, written as $\tilde{\mathbf{Q}}_h^{n+1} = (\tilde{h}_h^{n+1}, (\tilde{h}u)_h^{n+1}, (\tilde{h}w)_h^{n+1})^T$.

3.2 | Correction Step

First of all, note that there is no non-hydrostatic term in the mass equation. Therefore, no correction is made to it, i.e. $h^{n+1} = \tilde{h}^{n+1}$. The correction is then made to the momentum equations, which are solved based on the backward Euler method, following:

$$\frac{(hu)^{n+1} - (\tilde{h}u)^{n+1}}{\Delta t} = -\frac{1}{\rho} (\tilde{h}p^{nh})_x^{n+1} + \frac{d_x^{n+1}}{\rho} \left(\frac{6}{4 + (d_x^{n+1})^2} (p^{nh})^{n+1} + \frac{d_x^{n+1}}{4 + (d_x^{n+1})^2} (\tilde{h}p^{nh})_x^{n+1} + \phi^{n+1} \right), \quad (10)$$

$$\frac{(hw)^{n+1} - (\tilde{h}w)^{n+1}}{\Delta t} = \frac{1}{\rho} \left(\frac{6}{4 + (d_x^{n+1})^2} (p^{nh})^{n+1} + \frac{d_x^{n+1}}{4 + (d_x^{n+1})^2} (\tilde{h}p^{nh})_x^{n+1} + \phi^{n+1} \right), \quad (11)$$

with $\phi^{n+1} := \phi((d, \tilde{h}, \tilde{h}u)^{n+1})$. Through some manipulation, these last two equations yield an elliptic system of equations

$$(p^{nh})_x^{n+1} + \frac{2\tilde{h}_x^{n+1} - 3d_x^{n+1}}{2\tilde{h}^{n+1}} (p^{nh})^{n+1} + \frac{\rho(4 + (d_x^{n+1})^2)}{4\Delta t \tilde{h}^{n+1}} (hu)^{n+1} = \frac{4 + (d_x^{n+1})^2}{4\tilde{h}^{n+1}} \left(\phi^{n+1} d_x^{n+1} + \frac{\rho}{\Delta t} (\tilde{h}u)^{n+1} \right). \quad (12)$$

$$(hu)_x^{n+1} + \frac{3d_x^{n+1} - 2\tilde{h}_x^{n+1}}{2\tilde{h}^{n+1}} (hu)^{n+1} + \frac{3\Delta t}{\rho \tilde{h}^{n+1}} (p^{nh})^{n+1} = -2d_t^{n+1} - \frac{2(\tilde{h}w)^{n+1}}{\tilde{h}^{n+1}} - \frac{d_x^{n+1}(\tilde{h}u)^{n+1}}{2\tilde{h}^{n+1}} - \frac{\Delta t(4 + (d_x^{n+1})^2)}{2\rho \tilde{h}^{n+1}} \phi^{n+1}, \quad (13)$$

where $\phi^{n+1} := \phi((d, \tilde{h}, \tilde{h}u)^{n+1})$. These last two equations form an elliptic system of equations, which can be solved with the local discontinuous Galerkin (LDG) method. This method was initially developed by¹⁷ for a time-dependent, non-linear advection-diffusion system, which was further developed to solve the Poisson equation^{18,19} by rewriting it into a system of first-order equations, similar to what we have in Eq. 12 and 13. Furthermore, the correction to the vertical momentum is done based on the obtained corrected pressure.

Let us write Eq. 12 and 13 in a shorter form and neglect the superscript for simplicity as:

$$(p^{nh})_x + s_{11}(p^{nh}) + s_{12}(hu) = f_1, \quad (14)$$

$$(hu)_x + s_{21}(hu) + s_{22}(p^{nh}) = f_2. \quad (15)$$

Note that $s_{11} + s_{21} = 0$ and $s_{12} > 0$ in any case. These properties are important for the flux derivation, as stated in²⁰. This flux is the generalized form of the previously derived flux for the Poisson equation^{19,18}. The generalized flux can be expressed as:

$$(hu)_h^* = \{(hu)_h\} + c_{11}[p_h^{nh}] + c_{12}[u_h], \quad (16)$$

$$p_h^{nh*} = \{p_h^{nh}\} - c_{12}[p_h^{nh}] + c_{22}[u_h], \quad (17)$$

where $\{q\} = (q^- + q^+)/2$ and $[q] = q^- - q^+$ denote the neighboring element average and jump, with superscript $-$ and $+$ represent the value on the left and right element respectively. However, instead of setting $c_{11} = 1$ as in²⁰, we set $c_{11} = \frac{1}{2}$ to achieve the "flip-flop" behavior, which characterizes the LDG method. This lets us achieve a more efficient computation as it has more zero entries in its matrix form. To handle the boundary, we use the derived zero Dirichlet boundary conditions.

4 | PRELIMINARY RESULTS ON GLOBAL MODEL

Before developing the adaptive model, we investigate the validity of our numerical scheme by applying the extension globally on the whole computational domain. We begin with a simple propagating solitary wave. Thereafter, we test more complicated cases, where the waves are generated by a moving bottom, including those by vertical and horizontal movement. To quantitatively measure the accuracy of our model, we calculate the root mean square error (RMSE) of the water height to measure the error on the amplitude. Along with that, we also compute the Pearson correlation, denoted with r , to capture the waveform similarity. The latter index is crucial to show that our model produces the expected dispersive behavior.

4.1 | Solitary wave

This first benchmark considers a solitary wave propagating to the positive x -axis direction. Since our model is proven to be equivalent to the Serre equations for the flat bottom case, we can compare it to its analytical solution as given in²¹, expressed as:

$$\eta(x, t) = a \cosh^{-2}(K(x - ct - x_0)), \quad u(x, t) = \frac{c\eta(x, t)}{d + \eta(x, t)}. \quad (18)$$

This solution is suitable for a solitary wave with an amplitude of $a = 2 \text{ m}$ over a constant depth $d = 10 \text{ m}$, with a propagation velocity $c = \sqrt{g(d + a)}$ and a scaling factor $K = \sqrt{\frac{3a}{4d^2(d+a)}}$. In this case, the initial displacement is located at $x_0 = L/4$, where we consider a domain with a length of $L = 800 \text{ m}$.

For our simulation, we simply substitute $t = 0$ to Eq. 18 as our initial conditions for the water height and the horizontal momentum. The initial vertical momentum could further be calculated from Eq. 4. We run our simulation until $T = 30 \text{ s}$, where we discretize it with a time-step $\Delta t = 0.1 \text{ s}$ and element width $\Delta x = 4 \text{ m}$.

Fig. 1 compares our simulation with the analytical solution at the initial time $t = 0 \text{ s}$ and three timestamps $t = 10, 20, 30 \text{ s}$. Our numerical results match the analytical solution very well, with an RMSE of 0.0108 and correlation $r = 0.9997$ by the end of the simulation time. We note that the accuracy stems from the use of a quadratic pressure profile in the vertical, whereas a linear profile yields a notable inaccuracy in the amplitude for the same simulation time, as witnessed in^{11,12,14}.

4.2 | Impulsive vertical thrust

We investigate a more complicated test case, which involves a moving bottom. This benchmark is based on a laboratory experiment in²², where still water is disrupted by a vertical flip movement, generating a wave. We define a wall boundary condition next to the moving plate and an absorbing boundary on the other side. Mathematically, the bottom movement can be expressed as:

$$d(x, t) = h_0 - \zeta_0(1 - e^{-\alpha t})\mathcal{H}(b^2 - x^2), \quad (19)$$

where $h_0 = 0.05 \text{ m}$ represents the still water depth, $|\zeta_0| = 0.005 \text{ m}$ is the plate maximum displacement and $b = 0.61 \text{ m}$ is the plate's width. The movement of the plate follows the exponential equation, which depends on $\alpha = \frac{1.11}{t_c}$, where t_c being the characteristic time that fulfills $\frac{t_c \sqrt{gh_0}}{b} = 0.148$ and 0.093 for upward and downward case respectively.

To achieve a fair resolution with the measured data, we use $\Delta t = 0.01 \text{ s}$ and $\Delta x = 0.025 \text{ m}$. The comparison is made with the measured data at four measurement points $x = \{0.61, 1.61, 9.61, 20.61\} \text{ m}$, equivalent as $\frac{x-b}{h_0} = 0, 20, 180, 400$. The comparisons

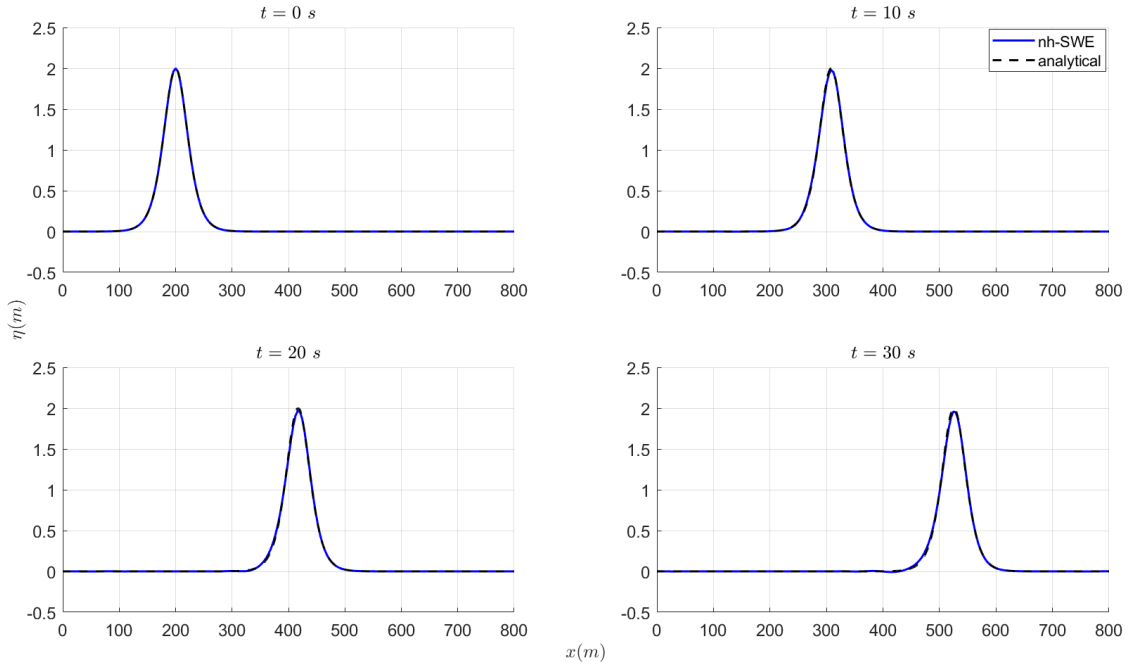


FIGURE 1 Comparison of our numerical simulation results (blue solid line) and its analytical solution (black dashed line) recorded at $t = 0, 10, 20, 30$ s.

are given in Fig. 2 and 3. All in all, it can be observed that our simulation results are in good agreement with the measured data, especially near the generation area $x = \{0.61, 1.61\}$ m. In particular, the phases of the dispersive wave trains are well captured by the simulation. Table 1 shows the quantitative comparisons with the measured data. From both cases, we can observe the dispersive behavior from our model, which also applies to the measured data. However, there is unavoidably a mismatch in the area away from the further measurement points $x = \{0.61, 1.61\}$ m, which is also the case in the previous studies with higher-order models^{4,22,23}. This might occur due to the viscous energy losses and boundary stresses in the experiments as suggested in²², which is neglected here and in all the mentioned studies.

Movement	RMSE				r			
	$\frac{x-b}{h_0} = 0$	$\frac{x-b}{h_0} = 20$	$\frac{x-b}{h_0} = 180$	$\frac{x-b}{h_0} = 400$	$\frac{x-b}{h_0} = 0$	$\frac{x-b}{h_0} = 20$	$\frac{x-b}{h_0} = 180$	$\frac{x-b}{h_0} = 400$
Uplift	0.0018	0.0022	0.0028	0.0063	0.9958	0.9936	0.9894	0.9589
Downdraft	0.0031	0.0029	0.0037	0.0064	0.9955	0.9902	0.9829	0.9609

TABLE 1 Root mean square error and correlation with respect to the measured data for each case.

4.3 | Sliding bump over flat bottom

This case also involves a moving bottom, yet with a horizontal movement. It follows an experimental setup in²⁴, exposed to a $h_0 = 0.175$ m still water level. The wave was generated by a sliding semi-elliptical aluminum block installed in the middle of the flume. A formulation of the bottom movement was proposed²⁵, written as:

$$d(x, t) = h_0 - H_s \left(1 - \left(\frac{2(x - S(t))}{L_s} \right)^4 \right), \quad S(t) - \frac{L_s}{2} < x < S(t) + \frac{L_s}{2}, \quad (20)$$

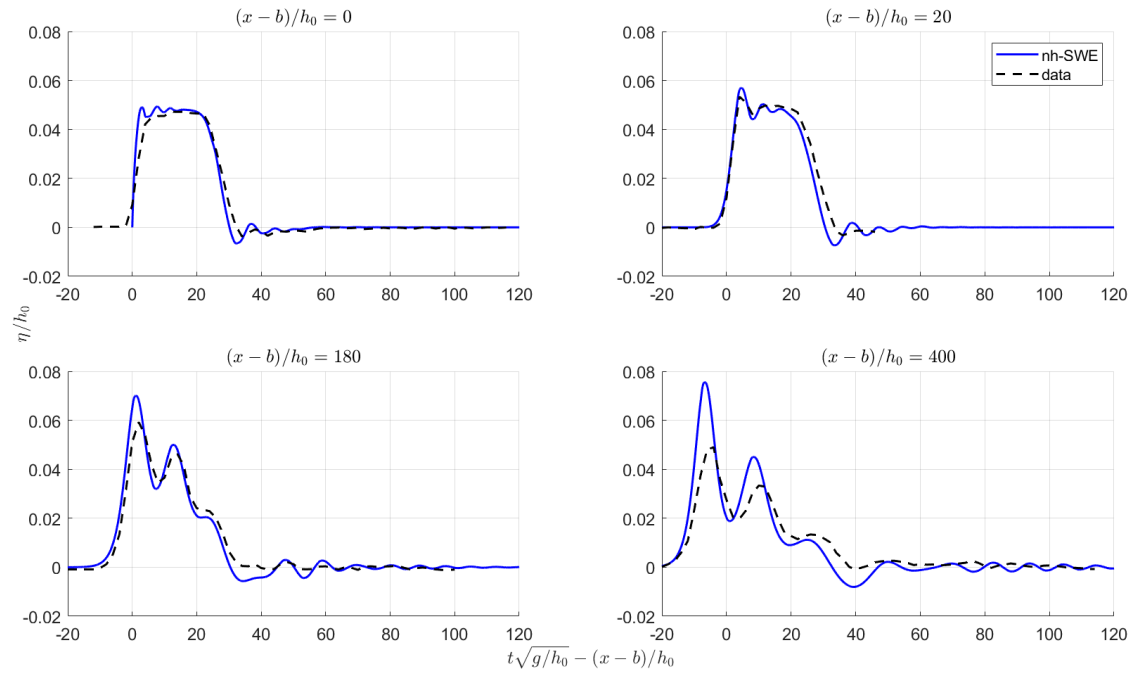


FIGURE 2 Comparison of the numerical simulations (blue solid line) and measured laboratory data (black dashed line) recorded at $x = 0.61, 1.61, 9.61, 20.61$ m for the uplift case.

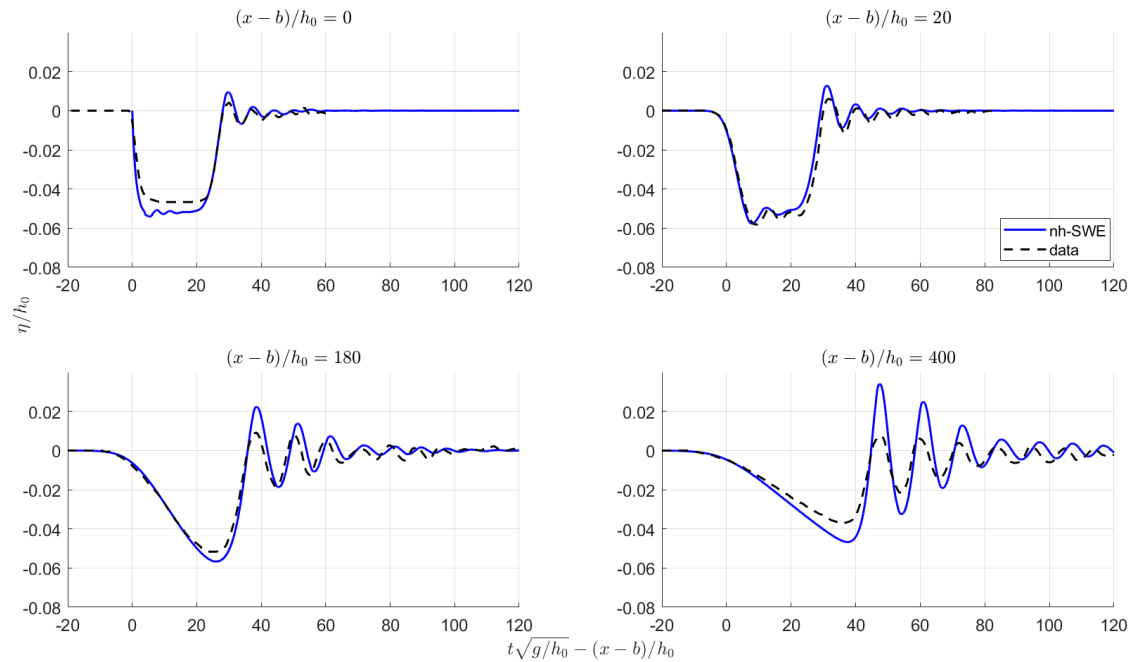


FIGURE 3 Comparison of the numerical simulations (blue solid line) and measured laboratory data (black dashed line) recorded at $x = 0.61, 1.61, 9.61, 20.61$ m for the downdraft case.

with $L_s = 0.5 \text{ m}$ and $H_s = 0.026 \text{ m}$ are being the slide height and thickness respectively. The movement of the slide is controlled by a function $S(t)$, given as:

$$S(t) = \begin{cases} \frac{1}{2}a_0t^2 & , 0 \leq t \leq t_1, \\ \frac{1}{2}a_0t_1^2 + u_t(t - t_1) & , t_1 < t \leq t_2, \\ \frac{1}{2}a_0t_1^2 + u_t(t - t_1) - \frac{1}{2}a_0(t - t_2)^2 & , t_2 < t \leq t_3, \\ \frac{1}{2}a_0t_1^2 + u_t(t_3 - t_1) - \frac{1}{2}a_0(t_3 - t_2)^2 & , t > t_3. \end{cases} \quad (21)$$

The comparison is made with three measured cases, following the parameters in Table 2 .

Fr	$a_0 \text{ (m/s}^2\text{)}$	$u_t \text{ (m/s)}$	$t_1 \text{ (s)}$	$t_2 \text{ (s)}$	$t_3 \text{ (s)}$
0.125	1.500	0.163	0.109	2.109	2.218
0.25	1.500	0.327	0.218	2.218	2.436
0.375	1.500	0.491	0.327	2.327	2.654

TABLE 2 Parameters of the experimental setup.

For our computational purpose, we discretize our model with $\Delta t = 0.005 \text{ s}$ and $\Delta x = 0.075 \text{ m}$. We compare our simulation with the measured data at $t = \frac{8}{\sqrt{g/L_s}} \text{ s}$ as shown in Fig. 4 . Our simulations generally agree well with the data, which is represented by the produced errors and their correlation as in Table 3 .

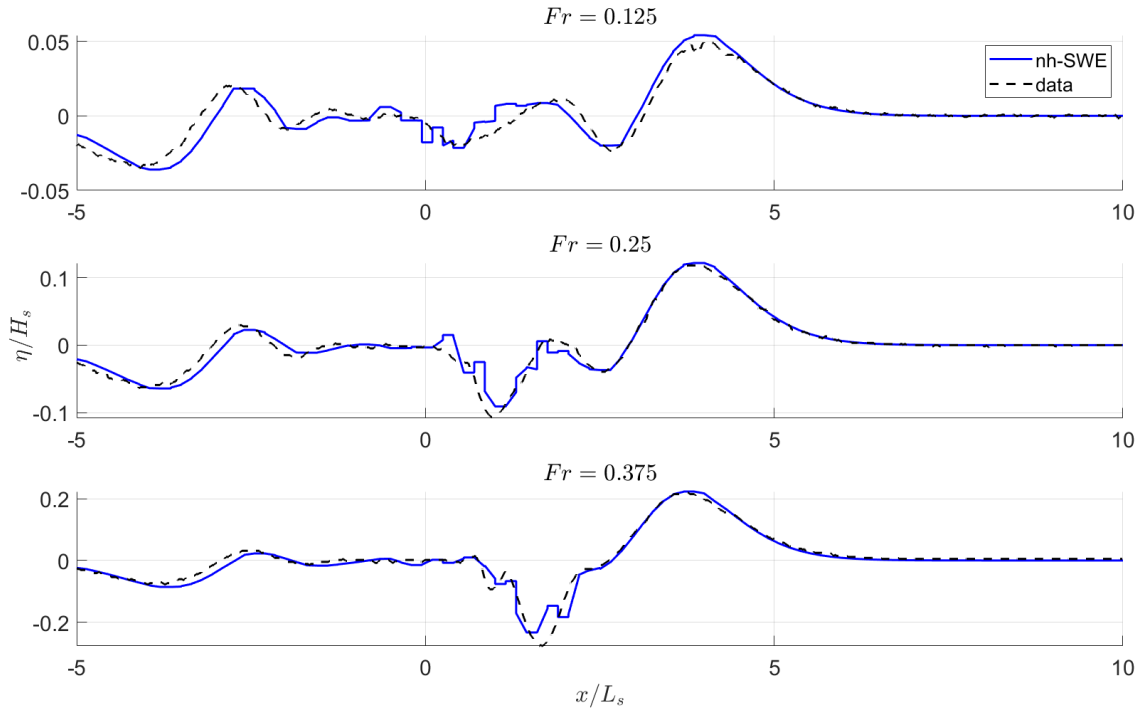


FIGURE 4 Comparison of the simulation result (blue solid line) with measured laboratory data (black dashed line) for a sliding semi-elliptic plate for $Fr = 0.125$ (top), 0.25 (middle), and 0.375 (bottom).

Fr	RMSE	r
0.125	0.0058	0.9530
0.25	0.0095	0.9750
0.375	0.0193	0.9732

TABLE 3 The produced error and correlation r with the measured data for each experimental setting

5 | TOWARDS ADAPTIVE MODEL

5.1 | Study on Adaptivity Criteria

In the previous part, we demonstrated the reliable and accurate modeling of weakly dispersive problems, including those generated by a moving bottom. As discussed earlier, the non-hydrostatic extension can be achieved by solving an elliptic system of equations based on the hydrostatic solution. Applying this correction globally results in an elliptic problem of the size equivalent to the number of all unknowns, requiring a correspondingly high computational cost. It is possible to solve this non-hydrostatic extension locally, thanks to the projection-based method. This means we restrict the non-hydrostatic region after the prediction step and only solve the elliptic equations in a sub-domain. To achieve that, a proper criterion is required to define this sub-domain. For assessing the accuracy, we will compare the adaptive model result similar to the previous evaluation. Moreover, we also measure the computational efficiency by comparing the computational time of the local and global application of the extension.

For determining the area, where the non-hydrostatic extension is to be applied, it would be ideal to measure the size of this part of the equation, and apply it only where it exceeds a certain threshold. This estimate, however, needs to be derived from the hydrostatic predictor solution. One choice is to take $\frac{d}{\lambda} > 0.05$ as a criterion, with λ being the wavelength. We derive this from one of the main assumptions of shallow water theory, i.e., $\lambda \gg d^{26}$. However, determining the wavelength is not easy, especially for a more complicated case. Even a simple solitary wave case would have an infinite wavelength by definition. Hence, we take a first guess criterion based on the hydrostatic surface elevation $\tilde{\eta}$ given as $\left| \frac{\tilde{\eta}}{d} \right|$, another basic assumption of shallow water theory. Furthermore, we investigate any other possible criteria such as $|\tilde{\eta}_x|$, $|\tilde{u}|$, $|\tilde{u}_x|$, $|\tilde{w}|$, and $|\tilde{w}_x|$, which all can be obtained from the predictor step. For further notation, we neglect the tilde for simplicity. With these criteria, we should only solve the elliptic problem on the area where the value of the respective criterion exceeds a threshold k_{nh} . We set $k_{nh} = 0.001$ for all our test cases.

5.1.1 | Solitary wave

To illustrate how our proposed adaptive model works, we begin with the simple solitary wave case as investigated in the former section. Fig. 5 shows snapshots of an adaptive simulation on a propagating solitary wave with adaptive criterion $\left| \frac{\eta}{d} \right| > k_{nh}$. Physically, this criterion yields application of the correction to the area where significant elevation exists, which is intuitively reasonable for the solitary wave. From this example, we can see how the proposed approach can reduce the computational effort with a smaller corrected region. Since an analytical solution is known, Fig. 6 shows the absolute errors of both global and local approaches at the end of the simulation time. It can be observed that the local adaptation manages to produce a similar accuracy. Differences are observable only at the interfaces between hydrostatic and non-hydrostatic regions. Note that the error is plotted for the discontinuous elements of the DG spatial discretization.

Criterion	$t_{\text{local}}/t_{\text{global}}$	RMSE	r
$ \eta/d $	0.1048	0.0105	0.9997
$ \eta_x $	0.1016	0.0136	0.9995
$ u $	0.2738	0.0108	0.9997
$ u_x $	0.1285	0.0158	0.9993
$ w $	0.1646	0.0123	0.9996
$ w_x $	0.0818	0.1146	0.9606

TABLE 4 Comparison of time ratio, errors, and correlations between the locally applied method and the analytical solution of propagating solitary wave with $k_{nh} = 0.001$ being the threshold.

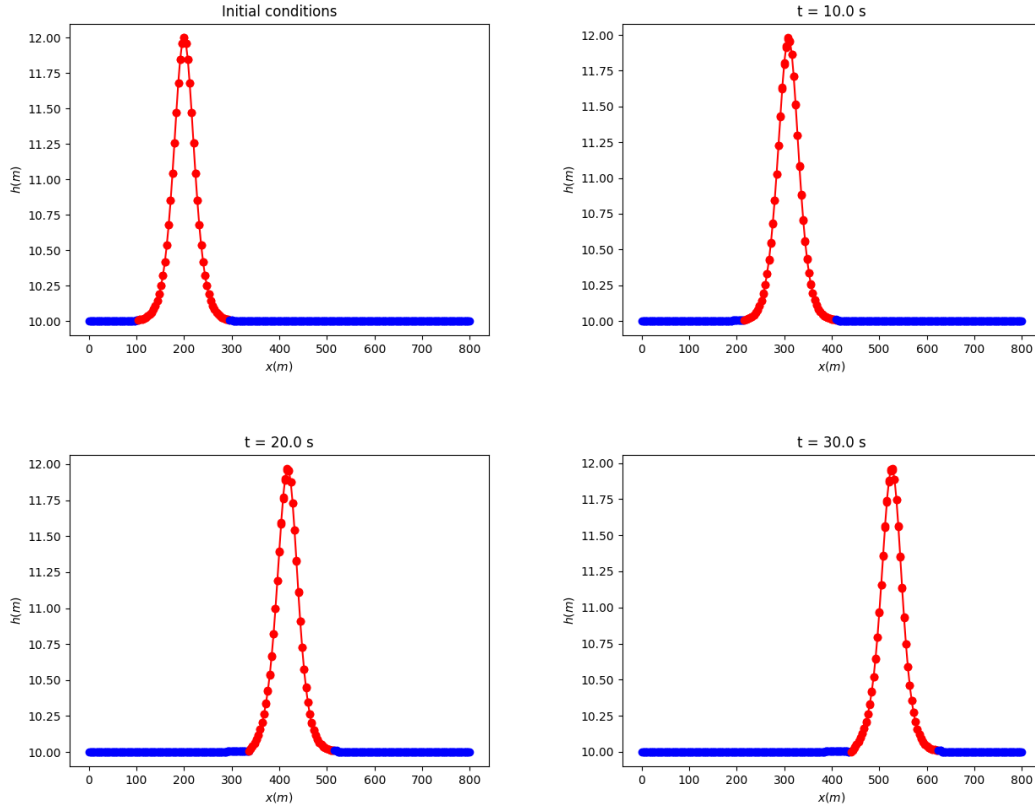


FIGURE 5 Illustration of adaptive simulation of a propagating solitary wave, with splitting criterion $\left| \frac{\tilde{\eta}}{d} \right| > k_{nh} = 0.001$. The blue area depicts the hydrostatic area, while the red represents the non-hydrostatic domain, where we apply the correction.

To compare the performance of the proposed criterion, Table 4 lists the computational time ratio, the RMSE, and the correlation to the analytical solution at the end of the simulation time. It can be observed that most proposed criteria match the analytical solution, with $\left| \frac{\tilde{\eta}}{d} \right|$ giving the least error, while only taking 10.48% of the global computational time (see Fig. 7 for illustration). In contrast, criterion $|w_x|$ gives relatively poor results in both metrics (RMSE and r). This could be due to the fact that the form of the vertical velocity has two critical points (where $w_x = 0$), which leads to isolated elements. The existence of these isolated elements potentially introduces the larger error.

5.1.2 | Impulsive vertical thrust

Note that in the next two cases, the initial vertical momentum value is zero, representing undisturbed water. However, this leads to static vertical momentum since the hydrostatic term also depends on the vertical momentum value from the previous step. Therefore, criteria $|w|$ and $|w_x|$ will not work. A slight modification is required for these two criteria, where we apply the model globally for one time-step and apply the model locally in the further steps. This approach allows a dynamic vertical momentum for the following steps.

Table 5 and 6 show results from each criterion for upward and downward movement, respectively. By summing up the errors from each measurement point and considering their correlations, criterion $\left| \frac{\tilde{\eta}}{d} \right|$ gives the best results compared to others. Fig. 8 and 9 depict the results by taking such a criterion. The local approach with criterion $\left| \frac{\tilde{\eta}}{d} \right|$ manages to capture the significant dynamics while only taking 6.81% and 8.79% of the global computation time for the upward and downward movement, respectively.

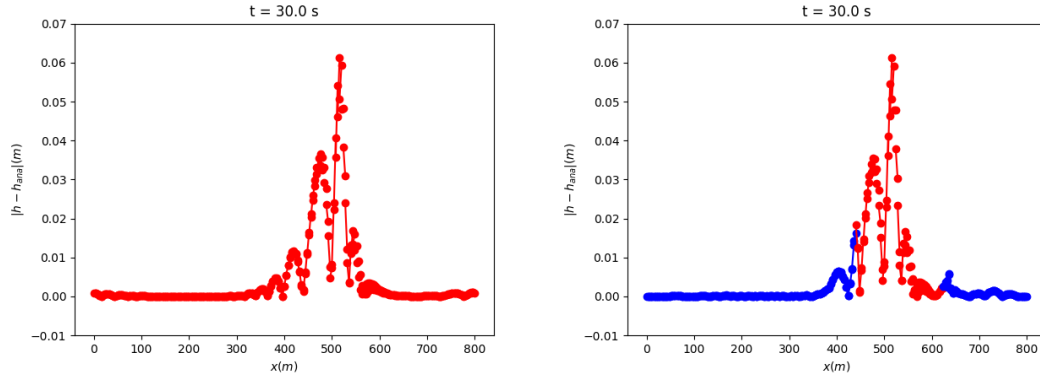


FIGURE 6 Comparison of the absolute error of the global (left) and local (right) approach on the propagating solitary wave test case, with splitting criterion $\left| \frac{\tilde{\eta}}{d} \right| > k_{nh} = 0.001$.

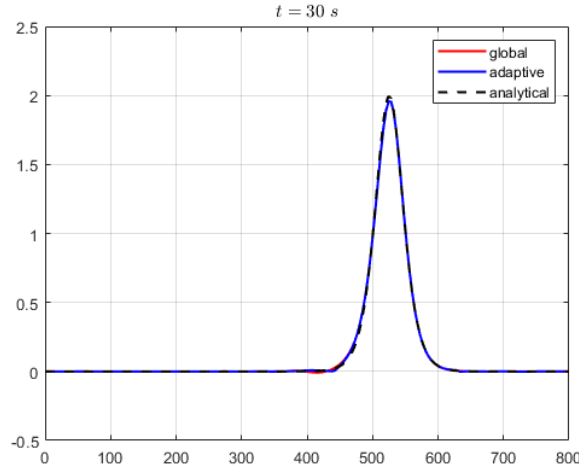


FIGURE 7 Comparison of the global simulation (red solid line), locally adaptive simulation (blue solid line) with the analytical solution (black dashed line), with criterion $\left| \frac{\tilde{\eta}}{d} \right| > k_{nh} = 0.001$

Criterion	$t_{\text{local}}/t_{\text{global}}$	RMSE				r			
		$\frac{x-b}{h_0} = 0$	$\frac{x-b}{h_0} = 20$	$\frac{x-b}{h_0} = 180$	$\frac{x-b}{h_0} = 400$	$\frac{x-b}{h_0} = 0$	$\frac{x-b}{h_0} = 20$	$\frac{x-b}{h_0} = 180$	$\frac{x-b}{h_0} = 400$
$ \eta/d $	0.0681	0.0018	0.0023	0.0029	0.0066	0.9955	0.9929	0.9876	0.9503
$ \eta_x $	0.0587	0.0023	0.0027	0.0040	0.0059	0.9925	0.9903	0.9707	0.9330
$ u $	0.1016	0.0022	0.0027	0.0034	0.0067	0.9931	0.9898	0.9819	0.9436
$ u_x $	0.0869	0.0021	0.0025	0.0036	0.0058	0.9938	0.9917	0.9758	0.9380
$ w $	0.0185	0.0019	0.0027	0.0051	0.0066	0.9948	0.9903	0.9534	0.9161
$ w_x $	0.0220	0.0030	0.0031	0.0052	0.0066	0.9871	0.9863	0.9529	0.9179

TABLE 5 Comparison of computational time ratio, errors, and correlations between the locally applied method and the measured laboratory data for the uplift vertical moving plate test case with $k_{nh} = 0.001$ being the threshold.

Criterion	$t_{\text{local}}/t_{\text{global}}$	RMSE				r			
		$\frac{x-b}{h_0} = 0$	$\frac{x-b}{h_0} = 20$	$\frac{x-b}{h_0} = 180$	$\frac{x-b}{h_0} = 400$	$\frac{x-b}{h_0} = 0$	$\frac{x-b}{h_0} = 20$	$\frac{x-b}{h_0} = 180$	$\frac{x-b}{h_0} = 400$
$ \eta/d $	0.0879	0.0034	0.0036	0.0037	0.0068	0.9928	0.9834	0.9841	0.9555
$ \eta_x $	0.0536	0.0040	0.0041	0.0042	0.0063	0.9888	0.9780	0.9708	0.9225
$ u $	0.2267	0.0037	0.0039	0.0044	0.0066	0.9912	0.9807	0.9755	0.9447
$ u_x $	0.1408	0.0037	0.0037	0.0038	0.0060	0.9915	0.9825	0.9765	0.9326
$ w $	0.0329	0.0033	0.0044	0.0050	0.0071	0.9927	0.9750	0.9597	0.9103
$ w_x $	0.0370	0.0043	0.0037	0.0050	0.0069	0.9855	0.9829	0.9584	0.9120

TABLE 6 Comparison of computational time ratio, errors, and correlations between the locally applied method and the measured laboratory data for the downward vertical moving plate test case with $k_{nh} = 0.001$ being the threshold.

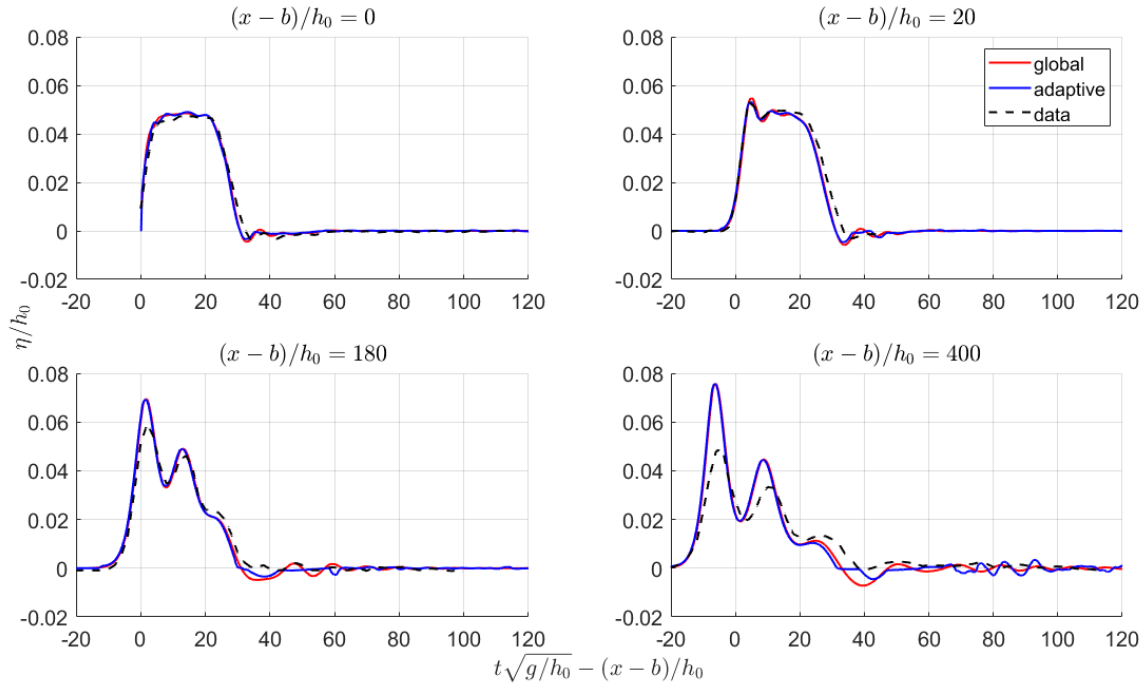


FIGURE 8 Comparison of the global simulation (red solid line), locally adaptive simulation (blue solid line), and measured laboratory data (black dashed line) recorded at $x = 0.61, 1.61, 9.61, 20.61$ m for the uplift case.

5.1.3 | Sliding bump over flat bottom

Finally, the adaptive simulation performance for the last test case can be seen in Table 7. In this case, however, the order of the performance of criteria $|w_x|$, $|\frac{\eta}{d}|$, and $|u|$ dominate these three cases interchangeably for both metrics. Out of curiosity, we illustrate comparing these three criteria in Fig. 10. It turns out that criterion $|w_x|$ mismatches the leading waveform, while the other two criteria match it well. However, it represents the following wave better, especially for a higher Froude number. In terms of computational time between these three criteria, criterion $|w_x|$ takes the shortest time, requiring 22.06 – 27.28% of the global computational time. Following that, criterion $|\frac{\eta}{d}|$ takes 30.65 – 37.39% of the global time, while $|u|$ requires 36.17 – 49.76%.

5.2 | Study on Improvement

Motivated by the observation in the solitary test case, where the error in the adaptive run compared to the global run occurred at the interfaces, to improve the adaptive model further, we experiment by enlarging the correction domain by one element both to the left and right of the non-hydrostatic sub-domain. This allows to avoid the isolated elements issue, such as the one that clearly

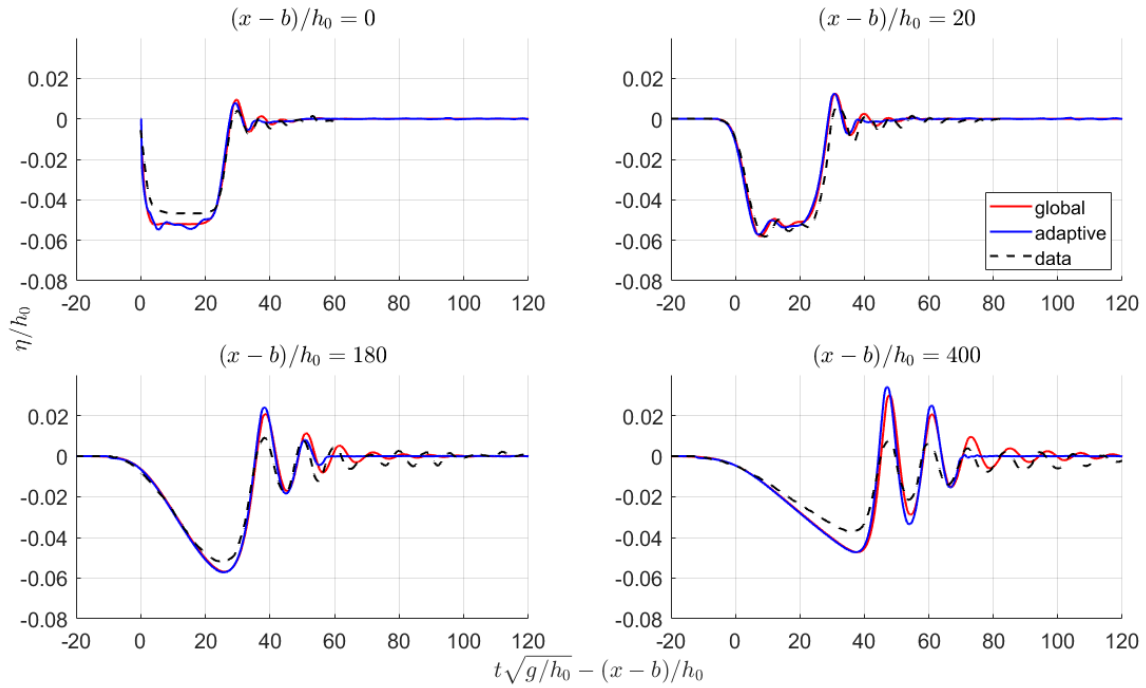


FIGURE 9 Comparison of the global simulation (red solid line), locally adaptive simulation (blue solid line), and measured laboratory data (black dashed line) recorded at $x = 0.61, 1.61, 9.61, 20.61$ m for the downdraft case.

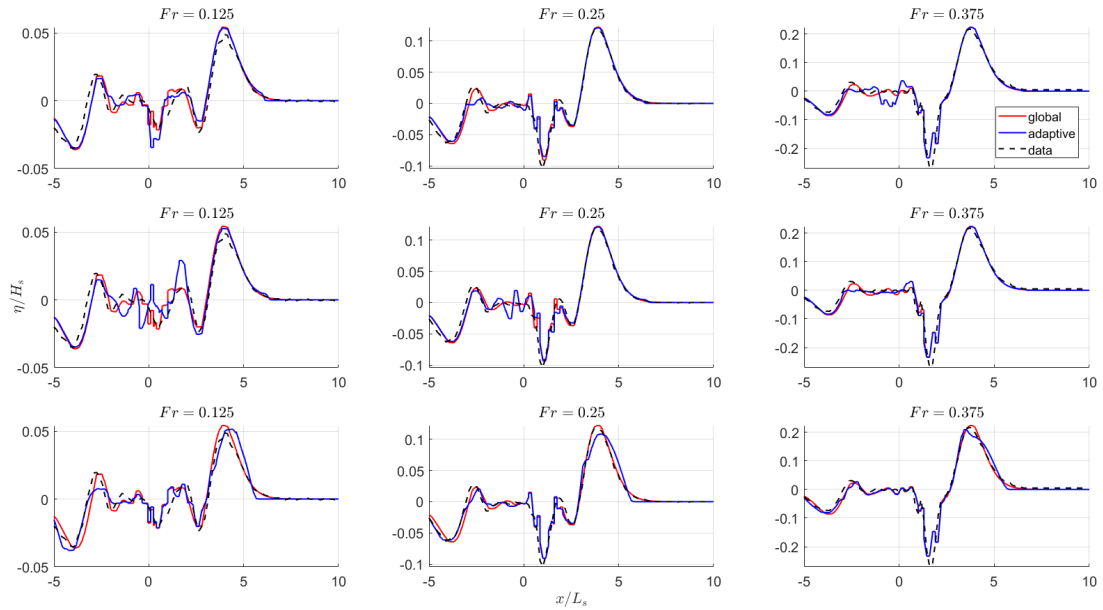


FIGURE 10 Comparisons of the global simulation (red solid line), locally adaptive model (blue solid line), with measured laboratory data (black dashed line) of the sliding bump test case, produced by criterion $\left| \frac{\eta}{a} \right|$ (top), $|u|$ (middle), and $|w_x|$ (bottom), with $k_{nh} = 0.001$ being the threshold.

$Fr = 0.125$				$Fr = 0.25$			
Criterion	$t_{\text{local}}/t_{\text{global}}$	RMSE	r	Criterion	$t_{\text{local}}/t_{\text{global}}$	RMSE	r
$ \eta/d $	0.3065	0.0064	0.9435	$ \eta/d $	0.3624	0.0103	0.9703
$ \eta_x $	0.2623	0.0093	0.8592	$ \eta_x $	0.2032	0.0488	0.6074
$ u $	0.4976	0.0079	0.9130	$ u $	0.3977	0.0108	0.9675
$ u_x $	0.4247	0.0083	0.8904	$ u_x $	0.3577	0.0218	0.8707
$ w $	0.0965	0.0205	0.5696	$ w $	0.0862	0.0290	0.7885
$ w_x $	0.2206	0.0060	0.9475	$ w_x $	0.2728	0.0117	0.9621

$Fr = 0.375$			
Criterion	$t_{\text{local}}/t_{\text{global}}$	RMSE	r
$ \eta/d $	0.3739	0.0224	0.9635
$ \eta_x $	0.2989	0.0236	0.9592
$ u $	0.3617	0.0201	0.9711
$ u_x $	0.3646	0.0502	0.8444
$ w $	0.0967	0.0473	0.8441
$ w_x $	0.2677	0.0208	0.9690

TABLE 7 Comparison of computational time ration, errors, and correlations between the locally applied method and the measured laboratory data for sliding bump over flat bottom test case with $Fr = 0.125$ (top-left), $Fr = 0.25$ (top-right), and $Fr = 0.375$ (bottom), where $k_{nh} = 0.001$ being the threshold.

occurs in the solitary wave using criterion $|w_x|$. Moreover, using zero non-hydrostatic Dirichlet boundary conditions, where the interface is tight to a non-zero value of the non-hydrostatic extension, may lead to a higher error on the interface between the corrected and non-corrected regions. Therefore, the idea of extending the adaptivity area could relax this interaction. Below are the results of applying such an enlargement.

5.2.1 | Solitary wave

Table 8 shows how enlarging the correction area by one element may overall improve the results by the proposed criteria, especially $|w_x|$. It can also be observed that the extension implies that all proposed criteria generally have similar accuracy to each other. Considering the computational time, criterion $\left|\frac{\eta}{d}\right|$ requires the least, taking only 15.93% of the global computational time.

Criterion	$t_{\text{local}}/t_{\text{global}}$	RMSE	r
$ \eta/d $	0.1593	0.0108	0.9997
$ \eta_x $	0.2555	0.0108	0.9997
$ u $	0.3820	0.0108	0.9997
$ u_x $	0.2946	0.0118	0.9996
$ w $	0.3953	0.0109	0.9997
$ w_x $	0.2884	0.0110	0.9997

TABLE 8 Comparison of computational time ratio, errors, and correlations between the enlarged locally applied method with the analytical solution of propagating solitary wave with $k_{nh} = 0.001$ being the threshold.

5.2.2 | Impulsive vertical thrust

This test case again shows how extending the correction domain can improve the accuracy of the proposed adaptive model, especially on the produced waveform, as shown in Table 9 and 10 for upward and downward movement, respectively. Most

proposed criteria give similar accuracies, with the exception of $|w|$, which clearly deviates based on the waveforms produced. This improvement comes with the cost of increased computational time, which is relatively significant compared to the previous test case due to the complexity of the dynamics. Criterion $\left|\frac{q}{d}\right|$ again demands the shortest computational time, with just 7.14% and 11.63% of the global application.

Criterion	$t_{\text{local}}/t_{\text{global}}$	RMSE				r			
		$\frac{x-b}{h_0} = 0$	$\frac{x-b}{h_0} = 20$	$\frac{x-b}{h_0} = 180$	$\frac{x-b}{h_0} = 400$	$\frac{x-b}{h_0} = 0$	$\frac{x-b}{h_0} = 20$	$\frac{x-b}{h_0} = 180$	$\frac{x-b}{h_0} = 400$
$ \eta/d $	0.0716	0.0018	0.0023	0.0029	0.0065	0.9953	0.9930	0.9878	0.9526
$ \eta_x $	0.4117	0.0021	0.0025	0.0031	0.0067	0.9939	0.9916	0.9850	0.9433
$ u $	0.4112	0.0055	0.0038	0.0035	0.0068	0.9578	0.9784	0.9818	0.9422
$ u_x $	0.4397	0.0019	0.0024	0.0030	0.0066	0.9947	0.9922	0.9869	0.9505
$ w $	0.3464	0.0018	0.0026	0.0050	0.0066	0.9954	0.9911	0.9556	0.9175
$ w_x $	0.4299	0.0022	0.0025	0.0028	0.0063	0.9930	0.9916	0.9894	0.9605

TABLE 9 Comparison of computational time ratio, errors, and correlations between the enlarged locally applied method and the measured laboratory data for the uplift vertical moving plate test case with $k_{nh} = 0.001$ being the threshold.

Criterion	$t_{\text{local}}/t_{\text{global}}$	RMSE				r			
		$\frac{x-b}{h_0} = 0$	$\frac{x-b}{h_0} = 20$	$\frac{x-b}{h_0} = 180$	$\frac{x-b}{h_0} = 400$	$\frac{x-b}{h_0} = 0$	$\frac{x-b}{h_0} = 20$	$\frac{x-b}{h_0} = 180$	$\frac{x-b}{h_0} = 400$
$ \eta/d $	0.1163	0.0034	0.0036	0.0037	0.0068	0.9932	0.9832	0.9848	0.9602
$ \eta_x $	0.6931	0.0035	0.0037	0.0035	0.0066	0.9923	0.9821	0.9870	0.9667
$ u $	0.6204	0.0035	0.0038	0.0038	0.0069	0.9921	0.9817	0.9830	0.9545
$ u_x $	0.8521	0.0034	0.0037	0.0035	0.0067	0.9931	0.9826	0.9876	0.9650
$ w $	0.6139	0.0031	0.0033	0.0055	0.0069	0.9948	0.9866	0.9516	0.9105
$ w_x $	0.6701	0.0035	0.0031	0.0040	0.0069	0.9931	0.9881	0.9802	0.9571

TABLE 10 Comparison of computational time ratio, errors, and correlations between the enlarged locally applied method and the measured laboratory data for the downdraft vertical moving plate test case with $k_{nh} = 0.001$ being the threshold.

5.2.3 | Sliding bump over flat bottom

Finally, Table 11 shows comparisons in our last test case of the sliding bottom. Expanding by one element homogenizes the results of most criteria with similar accuracy, with again the exception of $|w|$. The shortest simulation time was again achieved with criterion $\left|\frac{q}{d}\right|$ for all three different settings, which takes 37.6 – 40.32% of the global computational time.

6 | CONCLUSIONS

This research shows that a non-hydrostatic adaptive model can be achieved with a simple criterion based on the solution of the hydrostatic SWE. Simply enlarging the adaptation area by one element leads us to more accurate and consistent results. The adaptive model allows us to attain a similar accuracy to the global model while reducing more than 50% computational time. We plan to further investigate a more rigorous adaptive criterion and extend the applicability of this model to a two-dimensional and more realistic scenario. Involving the friction and viscosity terms are also of interest for further development.

$Fr = 0.125$				$Fr = 0.25$			
Criterion	$t_{\text{local}}/t_{\text{global}}$	RMSE	r	Criterion	$t_{\text{local}}/t_{\text{global}}$	RMSE	r
$ \eta/d $	0.3760	0.0061	0.9464	$ \eta/d $	0.4032	0.0094	0.9753
$ \eta_x $	0.4135	0.0057	0.9552	$ \eta_x $	0.5118	0.0095	0.9751
$ u $	0.5462	0.0057	0.9515	$ u $	0.4579	0.0092	0.9767
$ u_x $	0.5855	0.0059	0.9500	$ u_x $	0.5973	0.0096	0.9743
$ w $	0.2513	0.0205	0.5696	$ w $	0.2560	0.0290	0.7885
$ w_x $	0.5445	0.0058	0.9531	$ w_x $	0.6147	0.0095	0.9749

$Fr = 0.375$			
Criterion	$t_{\text{local}}/t_{\text{global}}$	RMSE	r
$ \eta/d $	0.4010	0.0192	0.9734
$ \eta_x $	0.5005	0.0193	0.9733
$ u $	0.5177	0.0191	0.9737
$ u_x $	0.5948	0.0191	0.9738
$ w $	0.2252	0.0471	0.8441
$ w_x $	0.6176	0.0193	0.9732

TABLE 11 Comparison of computational time ratio, errors, and correlations between the enlarged locally applied method and the measured laboratory data for sliding bump over flat bottom test case with $Fr = 0.125$ (top-left), $Fr = 0.25$ (top-right), and $Fr = 0.375$ (bottom), where $k_{nh} = 0.001$ being the threshold.

ACKNOWLEDGEMENTS

Part of this work is motivated by a Master's thesis by Leila Wegener at Universität Hamburg. The authors acknowledge the support of the Deutsche Forschungsgemeinschaft (DFG, German Research Foundation) within the Research Training Group GRK 2583 "Modeling, Simulation and Optimization of Fluid Dynamic Applications". J.B. additionally acknowledges funding by the DFG under Germany's Excellence Strategy – EXC 2037 "CLICCS - Climate, Climatic Change, and Society" – Project Number 390683824; as well as through the Collaborative Research Center TRR 181 "Energy Transfers in Atmosphere and Ocean" funded by the DFG - Project Number 274762653.

CONFLICTS OF INTEREST

The authors declare no conflicts of interest.

DATA AVAILABILITY STATEMENT

The data that support the findings of this study are available from the corresponding author upon reasonable request.

References

1. Glimsdal S, Pedersen GK, Harbitz CB, Løvholt F. Dispersion of tsunamis: does it really matter?. *Natural Hazards and Earth System Sciences* 2013; 13(6): 1507–1526. doi: 10.5194/nhess-13-1507-2013
2. Lynett P, Liu PLF. A numerical study of submarine–landslide–generated waves and run–up. *Proceedings of the Royal Society of London. Series A: Mathematical, Physical and Engineering Sciences* 2002; 458(2028): 2885–2910. doi: 10.1098/rspa.2002.0973

3. Ataie-Ashtiani B, Najafi Jilani A. A higher-order Boussinesq-type model with moving bottom boundary: applications to submarine landslide tsunami waves. *International Journal for Numerical Methods in Fluids* 2007; 53(6): 1019-1048. doi: 10.1002/fld.1354
4. Fuhrman DR, Madsen PA. Tsunami generation, propagation, and run-up with a high-order Boussinesq model. *Coastal Engineering* 2009; 56(7): 747-758. doi: 10.1016/j.coastaleng.2009.02.004
5. Dutykh D, Kalisch H. Boussinesq modeling of surface waves due to underwater landslides. *Nonlinear Processes in Geophysics* 2013; 20(3): 267-285. doi: 10.5194/npg-20-267-2013
6. Fang K, Liu Z, Sun J, Xie Z, Zheng Z. Development and validation of a two-layer Boussinesq model for simulating free surface waves generated by bottom motion. *Applied Ocean Research* 2020; 94: 101977. doi: <https://doi.org/10.1016/j.apor.2019.101977>
7. Peregrine DH. Long waves on a beach. *Journal of Fluid Mechanics* 1967; 27(4): 815-827. doi: 10.1017/S0022112067002605
8. Nwogu O. Alternative Form of Boussinesq Equations for Nearshore Wave Propagation. *Journal of Waterway, Port, Coastal, and Ocean Engineering* 1993; 119(6): 618-638. doi: 10.1061/(ASCE)0733-950X(1993)119:6(618)
9. Madsen PA, Schäffer HA. Higher-order Boussinesq-type equations for surface gravity waves: derivation and analysis. *Philosophical Transactions of the Royal Society of London. Series A: Mathematical, Physical and Engineering Sciences* 1998; 356(1749): 3123-3181. doi: 10.1098/rsta.1998.0309
10. Madsen PA, Bingham HB, Schäffer HA. Boussinesq-type formulations for fully nonlinear and extremely dispersive water waves: derivation and analysis. *Proceedings of the Royal Society of London. Series A: Mathematical, Physical and Engineering Sciences* 2003; 459(2033): 1075-1104. doi: 10.1098/rspa.2002.1067
11. Walters RA. A semi-implicit finite element model for non-hydrostatic (dispersive) surface waves. *International Journal for Numerical Methods in Fluids* 2005; 49(7): 721-737. doi: 10.1002/fld.1019
12. Stelling G, Zijlema M. An accurate and efficient finite-difference algorithm for non-hydrostatic free-surface flow with application to wave propagation. *International Journal for Numerical Methods in Fluids* 2003; 43(1): 1-23. doi: 10.1002/fld.595
13. Yamazaki Y, Kowalik Z, Cheung KF. Depth-integrated, non-hydrostatic model for wave breaking and run-up. *International Journal for Numerical Methods in Fluids* 2009; 61(5): 473-497. doi: 10.1002/fld.1952
14. Jeschke A, Pedersen GK, Vater S, Behrens J. Depth-averaged non-hydrostatic extension for shallow water equations with quadratic vertical pressure profile: equivalence to Boussinesq-type equations. *International Journal for Numerical Methods in Fluids* 2017; 84(10): 569-583. doi: 10.1002/fld.4361
15. Green AE, Naghdi PM. A derivation of equations for wave propagation in water of variable depth. *Journal of Fluid Mechanics* 1976; 78(2): 237-246. doi: 10.1017/S0022112076002425
16. Firdaus K, Behrens J. Non-Hydrostatic Model for Simulating Moving Bottom-Generated Waves: A Shallow Water Extension With Quadratic Vertical Pressure Profile. *International Journal for Numerical Methods in Fluids*; n/a(n/a). doi: <https://doi.org/10.1002/fld.5393>
17. Cockburn B, Shu CW. The Local Discontinuous Galerkin Method for Time-Dependent Convection-Diffusion Systems. *SIAM Journal on Numerical Analysis* 1998; 35(6): 2440-2463. doi: 10.1137/S0036142997316712
18. Cockburn B. Discontinuous Galerkin methods. *ZAMM - Journal of Applied Mathematics and Mechanics / Zeitschrift für Angewandte Mathematik und Mechanik* 2003; 83(11): 731-754. doi: 10.1002/zamm.200310088
19. Castillo P. A review of the Local Discontinuous Galerkin (LDG) method applied to elliptic problems. *Applied Numerical Mathematics* 2006; 56(10): 1307-1313. Selected Papers from the First Chilean Workshop on Numerical Analysis of Partial Differential Equations (WONAPDE 2004)doi: 10.1016/j.apnum.2006.03.016

20. Jeschke A. *Second Order Convergent Discontinuous Galerkin Projection Method for Dispersive Shallow Water Flows*. PhD thesis. Universität Hamburg, ; 2018
21. Seabra-Santos FJ, Renouard DP, Temperville AM. Numerical and experimental study of the transformation of a solitary wave over a shelf or isolated obstacle. *Journal of Fluid Mechanics* 1987; 176: 117–134. doi: 10.1017/S0022112087000594
22. Hammack JL. A note on tsunamis: their generation and propagation in an ocean of uniform depth. *Journal of Fluid Mechanics* 1973; 60(4): 769–799. doi: 10.1017/S0022112073000479
23. Xin Z, Shi Y, Zhang Y, Zhang Y. A One-Way Coupled Navier–Stokes–Serre Model for Simulating the Generation and Propagation of Tsunami Waves. *Pure and Applied Geophysics* 2024; 181(5): 1413-1426. doi: 10.1007/s00024-024-03485-1
24. Whittaker C, Nokes R, Davidson M. Tsunami forcing by a low Froude number landslide. *Environmental Fluid Mechanics* 2015; 15(6): 1215-139. doi: 10.1007/s10652-015-9411-6
25. Jing H, Chen G, Liu C, Wang W, Zuo J. Dispersive effects of water waves generated by submerged landslide. *Natural Hazards* 2020; 103(2): 1917-1941. doi: 10.1007/s11069-020-04063-z
26. Dean RG, Dalrymple RA. *Water Wave Mechanics for Engineers and Scientists*. WORLD SCIENTIFIC . 1991

